

Sparse wavefield reconstruction based on Physics-Informed neural networks

Bin Xu ^a, Yun Zou ^a, Gaofeng Sha ^b, Liang Yang ^c, Guixi Cai ^c, Yang Li ^{a,*}

^a School of Mechanical and Power Engineering, Zhengzhou University, Zhengzhou 450001, China

^b School of Advanced Manufacturing, Clover Park Technical College, Lakewood, Washington 98499, USA

^c Institute of Metal Research, Chinese Academy of Sciences, Shenyang 110016, China

ARTICLE INFO

Keywords:

Physics-Informed Neural Networks
Wavefield Reconstruction
Laser Ultrasonic
Non-destructive Testing

ABSTRACT

In recent years, the widespread application of laser ultrasonic (LU) devices for obtaining internal material information has been observed. However, this approach demands a significant amount of time to acquire complete wavefield data. Hence, there is a necessity to reduce the acquisition time. In this work, we propose a method based on physics-informed neural networks to decrease the required sampling measurements. We utilize sparse sampling of full experimental data as input data to reconstruct complete wavefield data. Specifically, we employ physics-informed neural networks to learn the propagation characteristics from the sparsely sampled data and partition the complete grid to reconstruct the full wavefield. We achieved 95% reconstruction accuracy using four hundredth of the total measurements. The proposed method can be utilized not only for sparse wavefield reconstruction in LU testing but also for other wavefield reconstructions, such as those required in online monitoring systems.

1. Introduction

Laser ultrasonic (LU) technology is a non-contact, visualized, and non-destructive testing (NDT) method, widely used in aerospace, automotive manufacturing, additive manufacturing, and other industries [1]. This technique involves using a pulsed laser beam to irradiate the sample surface, based on thermoelastic or ablation mechanisms, to generate ultrasonic wave signals [2]. These waves then travel through the sample and are captured by a laser interferometer or ultrasonic transducer. As a result, the internal structure, defects, and properties of the sample can be analyzed and evaluated using the ultrasonic wavefield. Compared to traditional ultrasonic testing, LU technology offers superior detection resolution and sensitivity, allowing for the identification of smaller defects. Furthermore, LU technology facilitates in-depth material inspection, effectively detecting both surface and subsurface flaws [3,4].

However, wavefield detection using LU technology is a time-consuming process. To reduce acquisition time without significantly compromising the accuracy of wavefield estimations, we need to either increase the repetition frequency of the pulsed laser or decrease the number of measurement samples. Increasing the repetition frequency is challenging, as higher frequency pulsed lasers are expensive, and the

wavefields from adjacent excitation points can easily overlap, causing confusion. Therefore, decreasing the number of measurement samples emerges as a more viable solution to reduce acquisition time. Traditionally, spatial sampling must adhere to the Nyquist-Shannon sampling criterion, which requires the spacing between samples to be less than half of the minimum wavelength [5]. Consequently, reconstructing sparse wavefields with fewer samples has become a prominent research focus.

In recent years, researchers have been continuously exploring and developing new methods and technologies to reconstruct the wavefield. Song et al. [6] proposed a method using compressive sensing technology to sparsely reconstruct wavefields. Under the Nyquist sampling criterion, they demonstrated a compression ratio of 90 %. The results indicate that the number of measurements required to measure the wavefield may be reduced by a factor of 10. Sabeti et al. [7] proposed a guided wave inversion method based on compressed sensing, which uses a two-dimensional ultrasonic guided wave model to reconstruct undersampled wavefields in both time and space domains. The results indicate that the proposed method can achieve over 80 % accuracy (in terms of correlation coefficient) with a spatiotemporal undersampling rate of approximately 40 %. Li et al. [8] developed an ultrasound field reconstruction technique for damage localization and imaging of metal plates

* Corresponding author.

E-mail address: yangli@zzu.edu.cn (Y. Li).

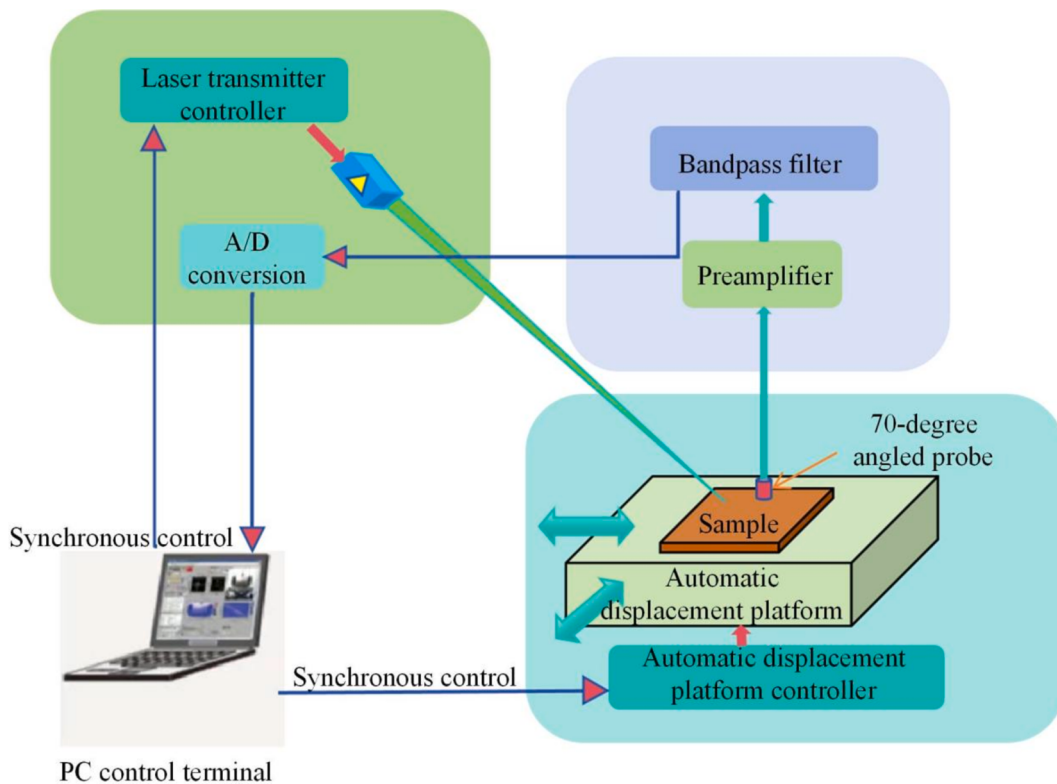


Fig. 1. Laser ultrasonic testing system.

by introducing compressive sensing methods. Liu et al. [9] proposed a multicomponent crossline wavefield reconstruction method based on sparse shearlet constraint inversion. The proposed method can effectively mitigate the multiplicity resulting from a limited number of samples by integrating the pressure wavefield with its crossline gradient. Gholami et al. [10] developed a simple method that halves the memory required for storing the forward wavefield needed for imaging conditions in the adjoint-state method. It only stored half of the wavefield at the Nyquist rate and calculated the second time derivative using the wave equation, allowing for the approximation of reconstructing the forward wavefield at the desired Nyquist rate. Even more so, Kalita et al. [11,12] proposed to represent the forward wavefield with the excitation time and amplitude to implement the adjoint method. Alguri et al. [13] employed an autoencoder neural network to acquire low-dimensional representations of wave propagation from numerical simulations. Subsequently, they fed a few experimental measurements into the neural network to reconstruct complete wave field data. They also demonstrated reconstruction accuracies of 86 % using only one-fourth of the total measurements. Azad et al. [14] proposed a convolutional neural network (CNN)-based pre-trained transfer learning method using ResNetV2 (RN2) model to solve the data scarcity problem. Li et al. [15] utilized autoencoders to achieve wavefield reconstruction from highly sparse wavefield data. Although there are many studies on reconstructing sparse wavefields, most are still simulation-based and adhere to the Nyquist sampling theorem. There is limited research on the reconstruction of highly sparse wavefields in the field of laser ultrasonic detection.

Physics-Informed Neural Networks (PINNs), proposed by Raissi et al. [16,17], provide an opportunity to address this problem. PINNs blend deep learning with physical information, and gaining significant attention recently in science and engineering. PINNs aim to guide neural networks training with physical constraints, leveraging neural networks' strengths in nonlinear mapping while maintaining the core principles of physical laws. This integration allows PINNs to understand complex physical systems without extensive labeled data, creating new

opportunities for scientific research and engineering applications. PINNs have been used for wavefield reconstruction. There are many studies on reconstructing wavefield in the time domain using PINNs. Song et al. [18] developed PINN-based WRI method and demonstrate its potential using a part of the Sigsbee2A model and a modified Marmousi model. Alkhalfah et al. [19] trained neural network (NN) models to be scattered wavefield solution functions of the Helmholtz equation and examine the role of the NN model size on the smoothness of these wavefields. Ren et al. [20] evaluated the role of PINNs in seismic wave propagation forward simulation through various numerical experiments. Majid et al. [21] proposed a PINNs algorithm applied to the two-dimensional acoustic wave equation. They tested this model through forward wave propagation and full wavefield inversion case studies, ultimately demonstrating that PINNs produced excellent results for inversion in all considered scenarios within limited computational complexity. Ding et al. [22] used self-adaptive PINNs combined with sparse initial wavefield data generated by the spectral element method to conduct numerical simulations of 2D SH wave propagation, aiming to achieve solutions for typical scenarios such as infinite/semi-infinite domains and arc-shaped canyon/hill topographies. Also mention the use of PINNs for sparse data applications, like PDE discovery and sparse data imaging [23–25].

This paper aims to explore the use of PINNs to reconstruct the LU wavefield from sparse measured data, obtained from LU experiments. Compared to previous wavefield reconstruction studies, the input data used in this study are more complex and subject to higher noise levels than the simulation data. The sparsely sampled data does not fully comply with the wave equation, and deviations at certain points during the training process may lead to larger errors in the results. We achieved 95 % reconstruction accuracy using four hundredth of the total measurements in this case. The organization of this paper is as follows: Section 2 elaborates on the process of LU experiments. Section 3 describes the preprocessing of experimental data. Section 4 outlines the theory of the two-dimensional wave equation and introduces the details of the PINNs network. Section 5 presents the results of wavefield

Table 1

The laser ultrasonic experimental parameters.

Laser Energy	Scanning Area	Scanning Interval	Sampling Frequency	Signal Length
1.20mJ	20 mm × 20 mm	0.20 mm	125 MHz	4000

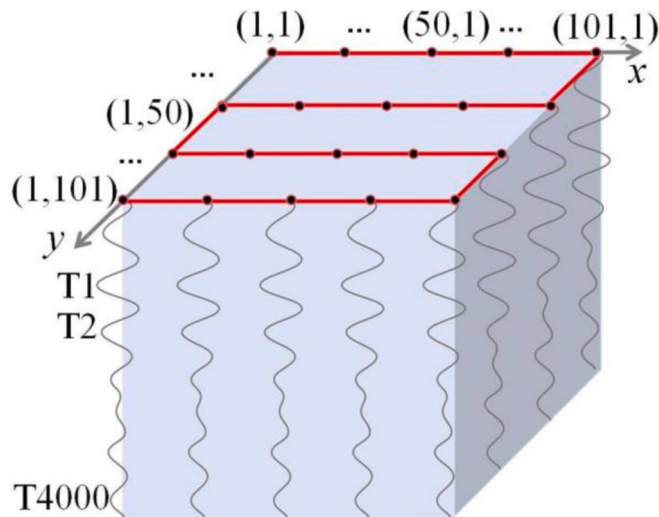


Fig. 2. The three-dimensional experimental data.

reconstruction. Additionally, a comparison is made between experimental data and PINNs prediction data, yielding favorable results. Finally, Section 6 summarizes this paper.

2. Laser ultrasonic experiments

The LU equipment used in this experiment is the LUVI-LL2 system from the Xi'an Jinbo Equipment Company. It includes a pulsed laser emitter, a stepper displacement platform, a X-Y-R platform, a band-pass filter, a signal acquisition card, and a computer interface. Fig. 1 shows schematic plot of the LU system.

The experimental material was a 200 mm × 200 mm × 3 mm aluminum alloy plate. The testing area was limited to 20 mm × 20 mm. A pulsed laser induced ultrasonic waves through the thermoelastic effect. The generated signal was received by a transducer at a 70° incident angle to detect the surface acoustic wave (SAW). SAW consists of two main types: Rayleigh waves and Love waves. Rayleigh waves involve elliptical particle motion, with displacement having both horizontal and vertical components. They are commonly excited and received using the

wedge or prismatic coupling block method, which converts longitudinal waves into Rayleigh modes at the surface [26]. Therefore, the angle transducer can receive the Rayleigh waves with the vertical components [27]. During testing, the specimen was positioned on a stepper displacement platform for precise control and motion recording. This platform allows for an upward movement of 400 mm in the x and y directions, with a displacement accuracy of 4 μm. Ultrasonic signals generated by the pulsed laser were recorded using an A/D acquisition card with a 125 MHz sampling frequency and a length of 4000 points. The scanning interval was 0.2 mm, resulting in a 101 × 101 point area (10,201 points). Table 1 details the LU setup parameters.

The wavefield data for grids are based on the collection of 10,201 channels, with a time interval of 8 ns within the channel, stored in a three-dimensional array of size $[N_x, N_y, N_t] = [101, 101, 4000]$, as illustrated in Fig. 2. This array comprises 10,201 channels, with each channel containing 4000 time sample points. The total duration of sampling is 32 μs.

Using the same method but changing the scanning interval, we repeated the above experiment. We set the scanning interval to 2 mm and 4 mm, resulting in three-dimensional data $[N_x, N_y, N_t] = [11, 11, 4000]$ and $[N_x, N_y, N_t] = [6, 6, 4000]$, respectively. Thus, we obtained three sets of experimental data with different scanning interval. Fig. 3 shows the wavefield of the three sets of data at the same time. Fig. 3a illustrates a time slice of the wavefield with a scanning interval of 0.2 mm, while Fig. 3b describes the time slice of the wavefield with a scanning interval of 2 mm, and Fig. 3c displays the wavefield time slice with a scanning interval of 4 mm. We can observe that compared to the wavefield time slice with a scanning interval of 0.2 mm, the wavefronts in the data with a scanning interval of 2 mm exhibit not really recognizable patterns. However, in the wavefield data with the scanning interval of 4 mm, there are almost no discernible wavefronts.

Fig. 4 shows the A-scan image at position (20, 20) on the x-y scanning plane of the Fig. 3a.

In order to further analyze the frequency domain characteristics of the SAW signal, a Fast Fourier Transform (FFT) was performed on it, and the resulting spectrum is shown in Fig. 4(b). From the spectrum, we can observe that the central frequency is approximately 1 MHz. The propagation velocity of SAWs in aluminum alloy materials is approximately 3000 m/s. According to the formula:

$$\lambda = \frac{c_p}{f} \quad (1)$$

where, λ represents the SAW wavelength, c_p represents the phase velocity, and f represents the central frequency of the SAW. Thus, the wavelength of the SAW is approximately 3 mm. Therefore, the scanning intervals for the three sets of experimental data are 1/15 λ , 2/3 λ , and 4/3 λ , respectively. The scanning intervals in Fig. 3b and 3c do not adhere to the Nyquist-Shannon sampling criterion, meaning the sparse wavefields do not capture the entire wavefield information. In the next

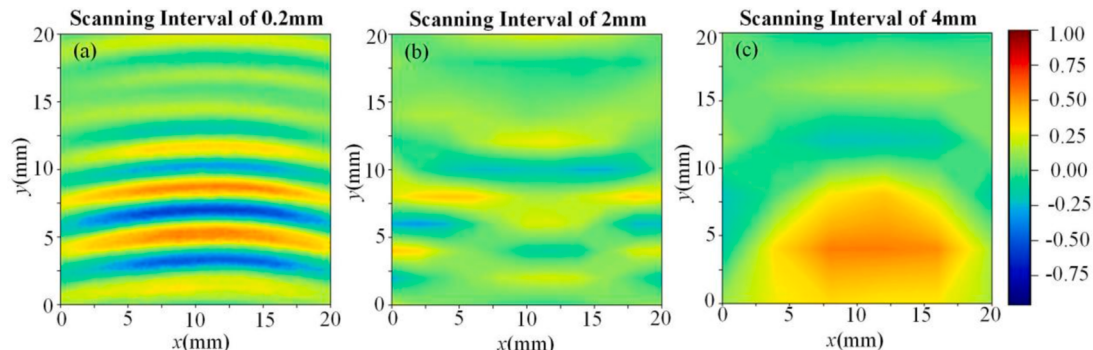


Fig. 3. Times slices of the wavefields with different scanning intervals: (a) with a scanning interval of 0.2 mm; (b) with a scanning interval of 2 mm; (c) with a scanning interval of 4 mm.

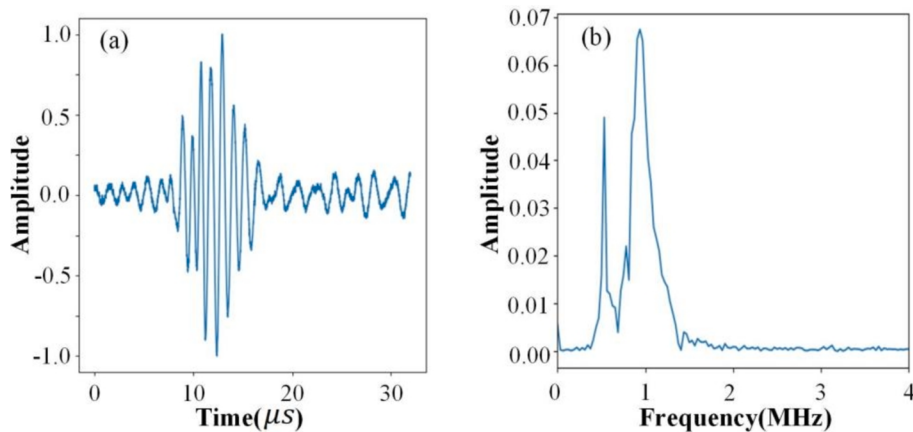


Fig. 4. (a) A-scan results and (b) the spectrum after apply FFT at position (20, 20) of the sample.

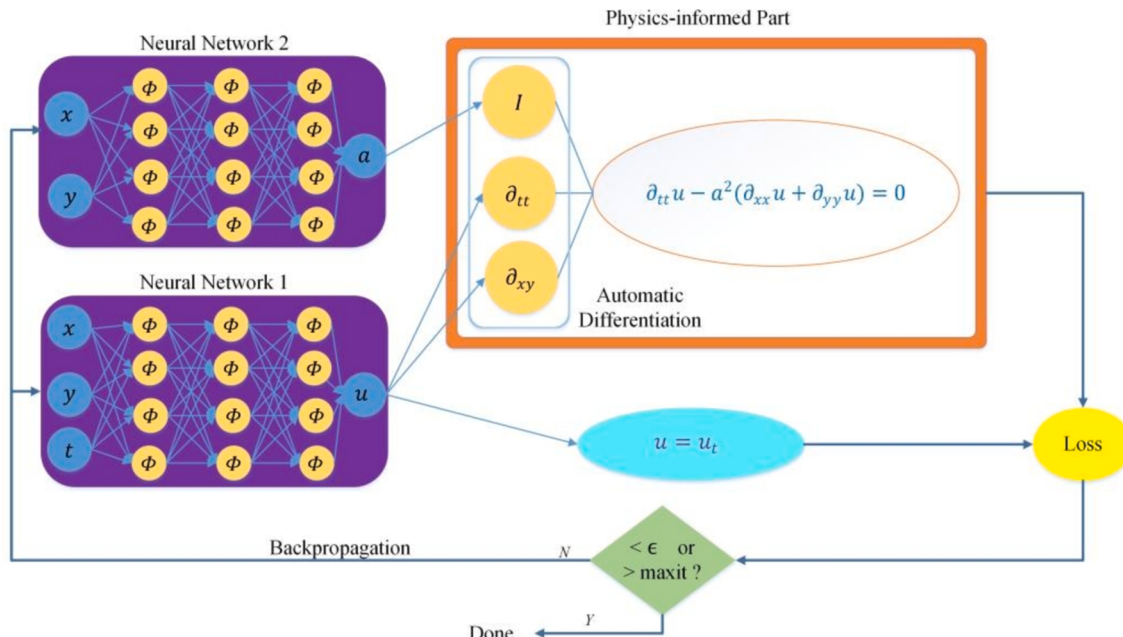


Fig. 5. Schematic of the PINNs' workflow. On the left, a fully connected feed-forward neural network generates outputs that approximate solutions to the forward problems. On the right, physical law and observed wavefield data are used to optimize the PINNs' parameters. The training ends when the error is less than a threshold ($\epsilon = 10$) or when the maximum number of iterations of the Backpropagation is reached.

section, we will use the PINN method to reconstruct the sparse wavefields.

3. Preprocessing of experimental data

To implement PINNs, a crucial normalization step is necessary to ensure convergence to the correct solution [28]. Thus, the experimental data must be mapped to the interval $[-1, 1] \in \mathbb{R}$ by the following method:

$$X \rightarrow \frac{X}{\max(|X|)} \quad (1)$$

where X means the amplitude of the time signals.

We further divided the grid coordinates for the three acquisition scenarios shown in the Fig. 2. The grid coordinate ranges for all three types of data are $(0, 1)$. For the data with the scanning interval of $1/15 \lambda$, the grid intervals are $dx = 0.01$, $dy = 0.01$, $dt = 0.00025$. For the data with the scanning interval of $2/3 \lambda$, the grid intervals are $dx = 0.1$, $dy = 0.1$, $dt = 0.00025$. For the data with the scanning interval of $4/3 \lambda$, the

grid intervals are $dx = 0.2$, $dy = 0.2$, $dt = 0.00025$.

We employ Physics-Informed Neural Networks (PINNs) to model sparse spatio-temporal coordinates and the corresponding real wavefield data. By performing wave equation calculations, we then derive the complete wavefield data. This approach ensures that PINNs learn the system's physical laws during training, allowing them to generate precise wavefield data in previously unobserved regions, thus achieving effective wavefield data reconstruction.

4. Physics-informed neural networks

4.1. Physical information in laser ultrasonic

We consider acoustic waves that propagate in a 2D medium characterized by minimal (basically no) density fluctuations and the absence of body forces; a scenario typical in LU testing. Such a wavefield can mathematically satisfy the following 2D wave equation [29]:

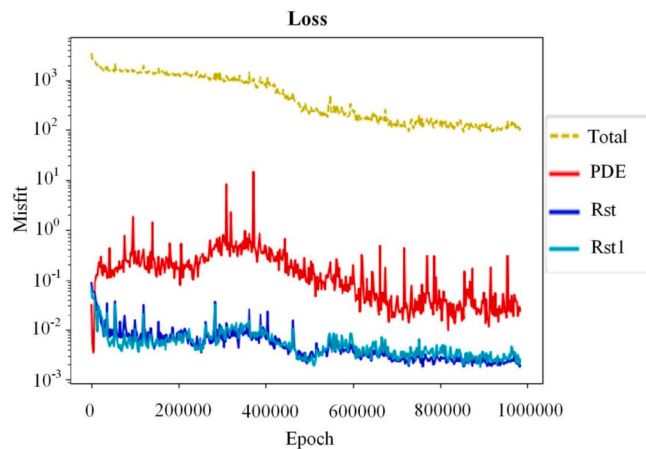


Fig. 6. Evolution of the different loss terms in equation (4) as well as the total loss. PDE, Rst and Rst1 correspond to the PDE, A-scan data loss terms and the A-scan data at the first point respectively.

$$\frac{\partial^2 u}{\partial t^2} - \alpha^2 \left(\frac{\partial^2 u}{\partial x^2} + \frac{\partial^2 u}{\partial y^2} \right) - f = 0 \quad (2)$$

where $u(x, y, t)$ denotes the pressure wavefield and $f(x, y, t)$ represents the source term. In most cases, such as in our experimental setup, f is set to zero. Here, α characterizes the acoustic wave speed. In this paper, the experimental material we used is homogeneous aluminum alloy plates, and the physical properties of the material do not change with coordinates. Therefore, this study does not consider variations in wave

speed.

Physics-informed neural networks (PINNs) utilize the inherent physical model to guide the training process. By integrating the wave equation into the neural network loss function, PINNs can learn the system's fundamental physics. This allows them to generate predictions that conform to both the observed data and the governing physical laws.

4.2. The components of PINN

In PINNs, a fully connected feed-forward neural network is the primary architecture used. The solution's derivatives with respect to the independent variables are computed via automatic differentiation, with frameworks like TensorFlow [30,31]. A linear transformation followed by a nonlinear neuron-wise activation function (σ) is applied on the input $x^{l-1} \in \mathbb{R}^{N_{l-1}}$ to the l^{th} layer:

$$x^l = \sigma(w^l x^{l-1} + b^l) \quad (3)$$

where $w^l \in \mathbb{R}^{N_l \times N_{l-1}}$ is the matrix of weights, and $b^l \in \mathbb{R}^{N_l}$ is the vector of biases corresponding to the l^{th} layer, and x^{l-1} is the input to the l^{th} layer. The successive operation of this transformation results in the final output of the neural network with a total number of $\sum_1^l N_l \times N_{l-1} + b^l$ tunable parameters. We employ the hyperbolic tangent activation function ($\sigma = \tanh(\bullet)$) across all neural networks utilized in this investigation [32]. The activation function applied to the output of the last hidden layer is the identity function, which implies that the last hidden layer is connected to the output via linear connections.

The parameters of the network are initiated from independent and identically distributed (iid) samples. The adjustable parameters in the PINNs are set up using the Xavier initial setting [33]. The weights and

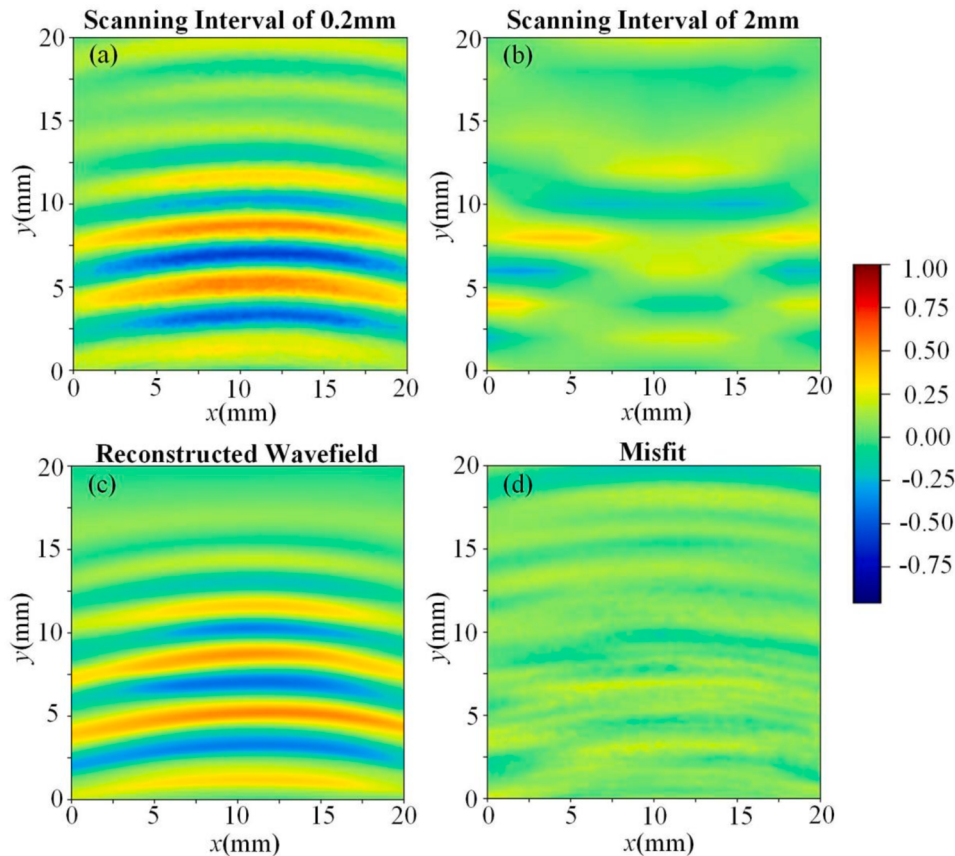


Fig. 7. Wavefield results at time instance = $14.08 \mu s$. (a) The wavefield with a scanning interval of $1/15 \lambda$, (b) the sparse wavefield used as input data, with a scanning interval of $2/3 \lambda$, (c) the wavefield reconstructed by PINNs using the sparse wavefield data shown in (b), and (d) the absolute pointwise error between (a) the real wavefield and (c) reconstructed wavefield.

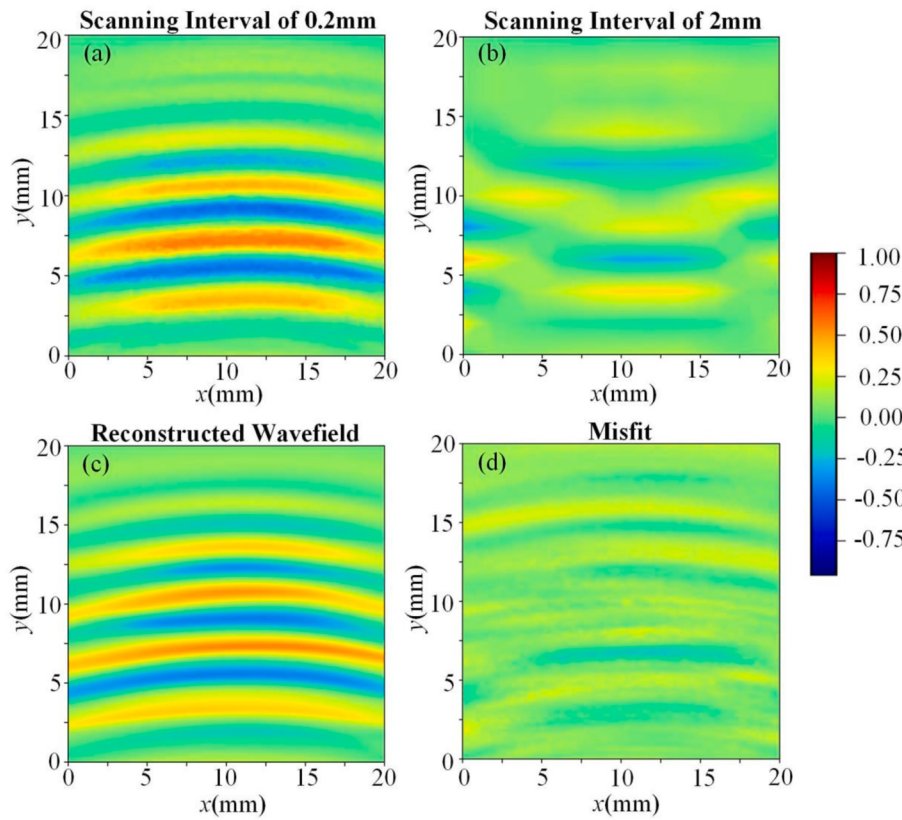


Fig. 8. Wavefield results at time instant $t = 14.72 \mu\text{s}$. (a) The wavefield with a scanning interval of $1/15 \lambda$, (b) the sparse wavefield used as input data, with a scanning interval of $2/3 \lambda$, (c) the wavefield reconstructed by PINNs using the sparse wavefield data shown in (b), and (d) the absolute pointwise error between (a) the real wavefield and (c) reconstructed wavefield.

biases are then optimized using the Adam optimization method [34,35].

We follow the standard framework of PINNs to derive parameters that closely approximate the scalar displacement $u(x,y,t)$. This involves embedding the partial differential equation within the neural network. The preprocessed input data is then fed into the neural network, allowing it to learn the rules of wave propagation. Subsequently, we define several residual terms that we aim to minimize [36].

PDE: $\frac{\partial^2 u}{\partial t^2} - a^2 \left(\frac{\partial^2 u}{\partial x^2} + \frac{\partial^2 u}{\partial y^2} \right)$ The partial differential equation

Rst: $u(x, t, y = 0) - u_z(x, t)$ The sparse wavefield data.

The neural network framework is depicted in Fig. 5. Two neural networks were created to compute displacement $u(x,y,t)$ and wave velocity a . Network 1 includes an input layer with three variables (x,y,t), six hidden layers with 64 neurons each, and an output layer. Neural Network 1: x, y, t (spatial and temporal coordinates), representing the input variables of the problem. $u(x,y,t)$, representing the output of the neural network, which is the solution of the system.

The initial section of Network 1 accepts the space-time coordinates of the A-scan data at the infrequent 11×11 (or 6×6) points of the wavefield as input data. It produces output equivalent to the associated displacement values u_t (where u_t is the experimental data) at that precise moment.

The Sobol' sequence algorithm was utilized for the spatial-temporal sampling of the PDE loss term, with random sampling within the space $x \in (0, 1)$, $y \in (0, 1)$, $t \in (0, 1)$ [37]. A total of 4×10^6 data points are picked in the three-dimensional space and used as input for the second part of Network 1. With each iteration, 100 sets of data are processed by Network 1, establishing a batch size of 100. Following this, the output is included in the computation of the partial differential equation. The central partial differential equation is a physical constraint, representing the condition that the physical system must satisfy. δ_{tt} and δ_{xy} represent the partial derivatives with respect to time and space, computed using

automatic differentiation. The training ends when the error is less than a threshold ϵ ($\epsilon = 10$) or when the maximum number of iterations is reached. For example, by choosing the grid point ($x = 0.35$, $y = 0.55$, $t = 0.45$) and feeding it into Network 1, the output u is engaged in the mathematical computation of the partial differential equation. The partial differential equation can therefore determine the normalized displacement value at the location ($x = 0.35 \times 20 \text{ mm}$, $y = 0.55 \times 20 \text{ mm}$) in the wavefield at the time $t = 14.08 \mu\text{s}$.

The design of Network 2 encompasses an input layer that holds two input variables (x,y), representing spatial coordinates, two hidden layers each with 64 neurons, and an output layer (a), representing the wave speed. It receives input in the form of spatial coordinates from the entire wavefield grid.

The variables $u(x,y,t)$ and $a(x,y)$ work together in the computation of the partial differential equation, which allows for the estimation of the displacement $u(x,y,t)$ over the complete set of [101, 101, 4000] grid coordinates. Since the experimental specimen is an aluminum alloy plate, we assume it to be a homogeneous material with constant density. Therefore, variations in wave speed are negligible in this study.

The loss function consists of two components: the error between the actual values and predicted values of the A-scan data at sparse 11×11 (or 6×6) point of the wavefield, and the error computed from the partial differential equation. The objective of the training process is to minimize the sum of mean squared errors [36]:

$$MSE(\Theta) = \lambda_1 MSE_{PDE} + \lambda_2 MSE_{st} \quad (4)$$

where $\Theta = W \cup b$ is the union of all the weights and biases of the neural network.

$$MSE_{PDE} = \frac{1}{N_{PDE}} \sum_{i=1}^{N_{PDE}} |R_{PDE}(x_i, y_i, t_i)|^2 \quad (5)$$

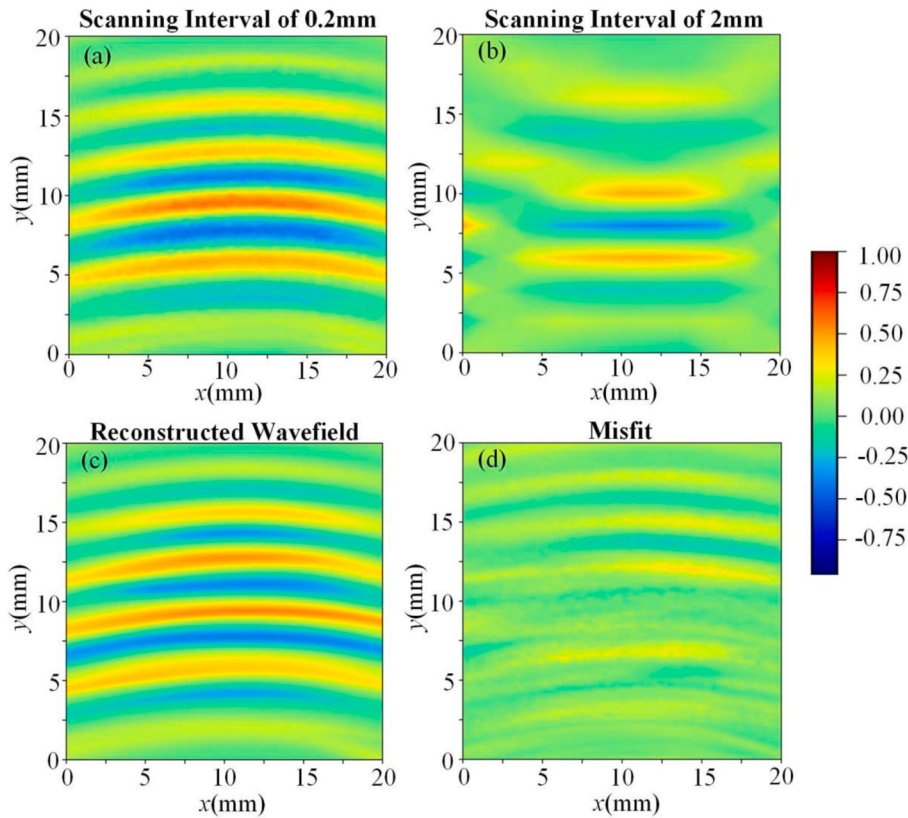


Fig. 9. Wavefield results at time instance $t = 15.36 \mu s$. (a) The wavefield with a scanning interval of $1/15 \lambda$, (b) the sparse wavefield used as input data, with a scanning interval of $2/3 \lambda$, (c) the wavefield reconstructed by PINNs using the sparse wavefield data shown in (b), and (d) the absolute pointwise error between (a) the real wavefield and (c) reconstructed wavefield.

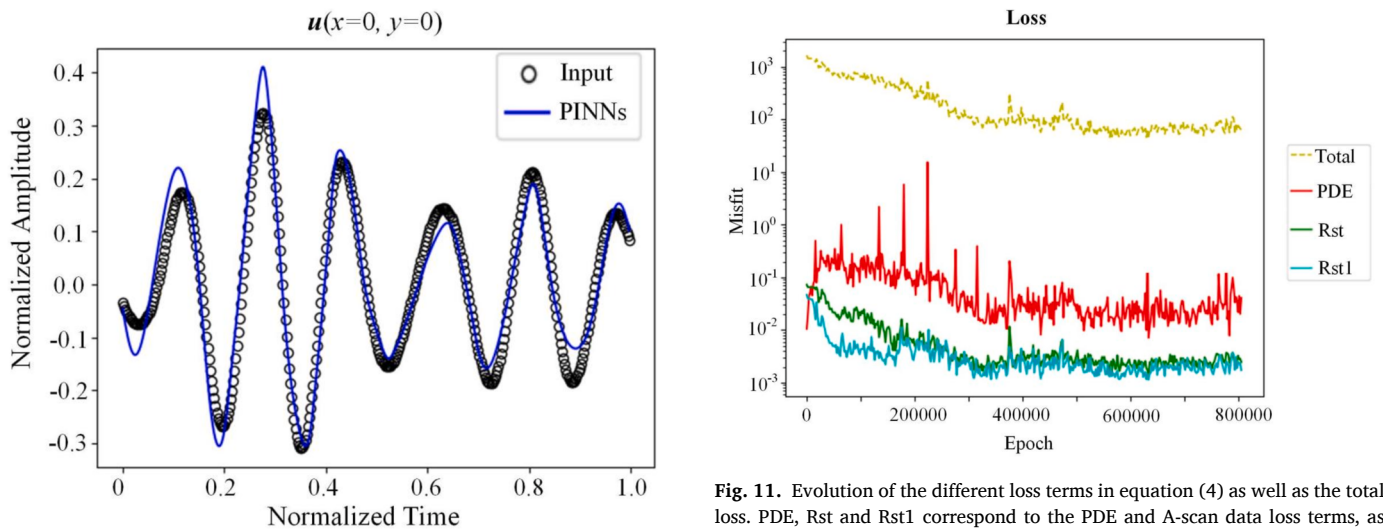


Fig. 10. The fitting results of the A-scan data at the first point among the 101 points selected of the wavefield. 'O' represents real data, the blue curve is the prediction of PINNs.

Table 2
Pearson correlation coefficients at different instance.

Time (μs)	14.08	14.72	15.36
PCC	0.950	0.956	0.950

which pertains to the loss term associated with the partial differential equation evaluated on a collection of randomly selected PDE input data $(x_i, y_i, t_i) \subset \Omega = \mathbb{R}^2 \times \mathbb{R}$, and x and y both belong to the range of 0 to 1. Similarly, the A-scan data loss term is defined as:

$$MSE_{st} = \frac{1}{N_{st}} \sum_{i=1}^{N_{st}} |R_{st}(x_i, y_i, t_i)|^2 \quad (6)$$

The hyperparameters $\lambda_{1,2} > 0$ in equation 4 are adjusted to normalize various loss terms, ensuring convergence to the correct solution. If the

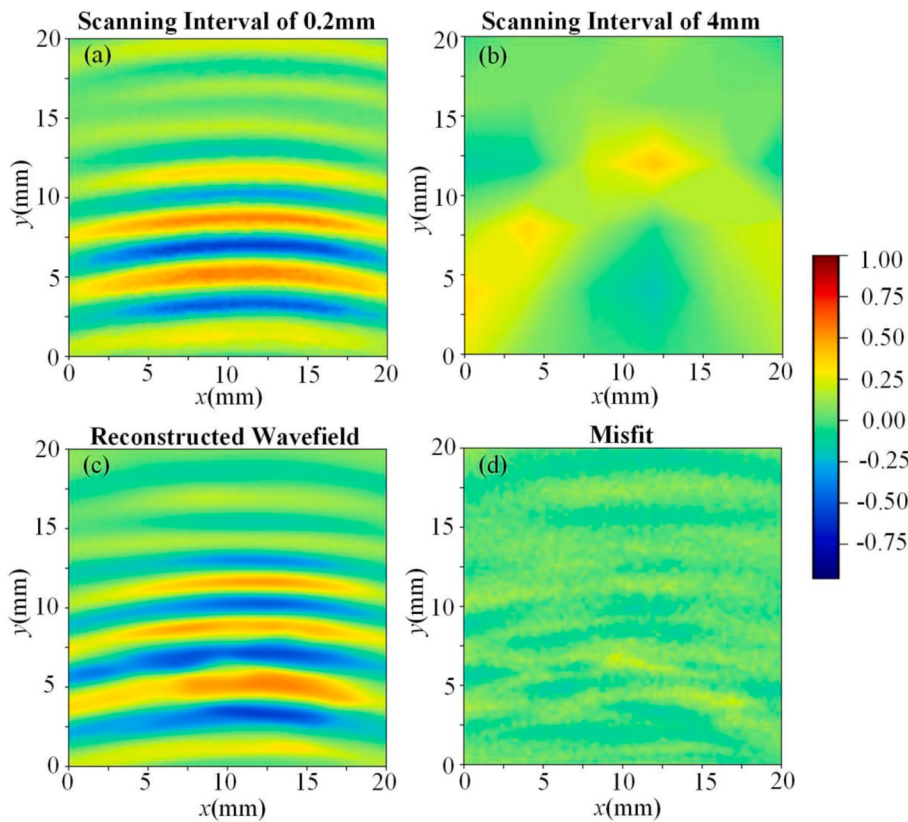


Fig. 12. Wavefield results at time instant $t = 14.08 \mu\text{s}$. (a) The wavefield with the scanning interval of $1/15 \lambda$, (b) the sparse wavefield with the scanning interval of $4/3 \lambda$ as the input data, (c) the reconstructed wavefield by PINNs, and (d) the absolute pointwise error between (a) the true wavefield and (c) reconstructed wavefield.

appropriate loss terms are not selected, it may result in delayed convergence or convergence to an incorrect solution. As commonly practiced in the literature on PINNs, the suitable values for $\lambda_{1,2}$ are determined heuristically through trial and error.

5. Results and discussion

5.1. Reconstruction of wavefield data with a scanning interval of $2/3\lambda$

We first test the ability of our proposed approach in the reconstruction of wavefield data with the scanning interval of $2/3\lambda$. The selection of hyperparameters plays a pivotal role in the training process of PINNs, as they directly influence the convergence and performance of the model. In our study, we tuned the hyperparameters $\lambda_1 = 20$, $\lambda_2 = 7000$, to strike a balance between effectively minimizing the loss function and preventing overfitting. Selecting these hyperparameters balances the fidelity of the reconstructed wavefield with the regularization from the physical constraints in the PINNs framework. Tuning them requires careful consideration of the weights in the loss function. For example, λ_1 controls the importance of satisfying the partial differential equation (PDE) constraints, ensuring the predicted wavefield aligns with wave propagation physics. Meanwhile, λ_2 influences the fidelity of the reconstructed wavefield by penalizing deviations from the sparse wavefield data.

Fig. 6 sheds light on the convergence behavior of the PINNs model during training. By tracking the changes in various loss terms over iterations, we gain a clear understanding of the model's learning dynamics and the effectiveness of the chosen hyperparameters. The convergence of loss terms to a minimum demonstrates the model's ability to capture data patterns and reduce prediction errors. Moreover, visualizing loss evolution helps identify issues like overfitting or underfitting. A rapid decrease in total loss, followed by stabilization or

minimal improvement in individual loss components, might indicate convergence to a suboptimal solution. The total loss gradually decreases; although the PDE loss function increases initially, it quickly converges later on; other loss terms also converge gradually; this may indicate convergence to a suboptimal solution.

Fig. 7 provides a detailed comparison between the true LU wavefield and the reconstructed wavefield using the PINNs method at a specific time instance, $t=14.08 \mu\text{s}$. In Fig. 7a, the LU wavefield with the scanning interval of $1/15 \lambda$ serves as the ground truth, acquired through LU testing methods, providing a reference for the accuracy of the reconstruction. Fig. 7b illustrates the sparse LU wavefield with the scanning interval of $2/3 \lambda$, representing the input data utilized by the PINNs model. Although some waveforms are shown in Fig. 7b, they appear relatively blurred, making it difficult for signal analysis. Fig. 7c shows the wavefield reconstructed by the PINNs. We can see that the reconstructed waveforms are relatively smooth. Fig. 7c also reveals some discrepancies between the true and reconstructed wavefields, as depicted in Fig. 7d, which shows the absolute pointwise error. We can see that the top of the wavefield has larger errors, displaying light blue streaks. However, considering the inherent background noise in LU experiments, the observed errors remain within an acceptable range, highlighting the robustness and reliability of the reconstructed wavefield generated by the PINNs method.

Figs. 8 and 9 present the reconstructed wavefields at two additional time instances, $t=14.72 \mu\text{s}$ and $t = 15.36 \mu\text{s}$, respectively. By conducting a comprehensive assessment of the PINNs' ability to reconstruct wavefields at different temporal snapshots, we gain a deeper understanding of the model's performance in capturing the dynamic wave propagation phenomena over time by examining the wavefields at multiple time instances. From Figs. 7, 8, and 9, we can see that as time progresses, surface waves gradually propagate upward. Moreover, compared to Fig. 7c, the errors shown in Fig. 8c and 9c are more evenly distributed.

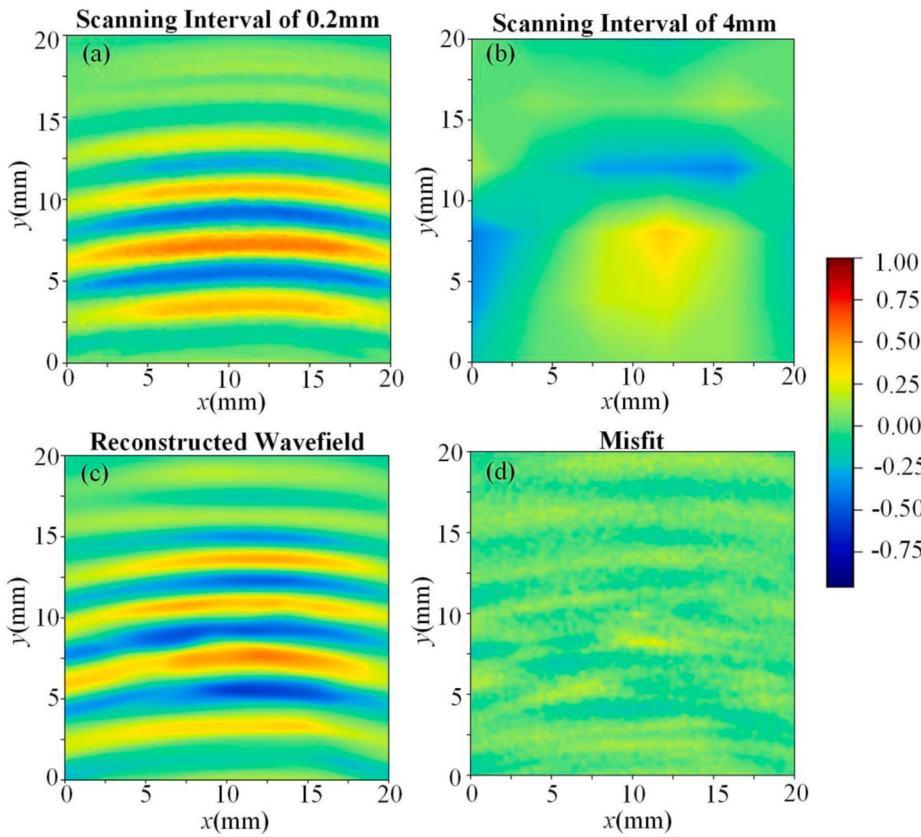


Fig. 13. Wavefield results at time instance $t = 14.72 \mu\text{s}$. (a) The wavefield with the scanning interval of $1/15 \lambda$, (b) the sparse wavefield with the scanning interval of $4/3 \lambda$ as the input data, (c) the reconstructed wavefield by PINNs, and (d) the absolute pointwise error between (a) the true wavefield and (c) reconstructed wavefield.

Fig. 10 provides an overview of the PINNs model's fitting performance on the A-scan data collected at the first point among the sparse 11×11 wavefield points. By comparing the input signals with the predictions made by the PINNs model, we can evaluate its accuracy in capturing and reproducing the underlying characteristics of the A-scan data.

As shown in **Fig. 10**, the results produced by the PINNs model closely align with the input signals, demonstrating high fidelity in reproducing the observed data. This match between the input signals and the PINNs predictions highlights the model's effectiveness in capturing the essential features of the A-scan data, such as signal shape, frequency content, and temporal dynamics. Additionally, the PINNs model subtly adjusts the signal amplitudes based on the physical constraints of wave propagation. This ensures consistency with the expected behavior dictated by the physics-informed constraints within the model architecture. By adhering to the principles governing wave propagation, the PINNs model not only accurately reproduces the observed data, but also maintains coherence with the underlying physical phenomena.

To quantitatively evaluate the accuracy of the reconstructed wavefields, we introduce Pearson correlation coefficient(PCC) [38]. We compute the PCC between the true wavefield and the reconstructed wavefield.

$$PCC = \frac{\Sigma(X - \bar{X})(Y - \bar{Y})}{\sqrt{\Sigma(X - \bar{X})^2 \Sigma(Y - \bar{Y})^2}} \quad (7)$$

where X and Y represent the data sequences of the true wavefield and the reconstructed wavefield, respectively. \bar{X} and \bar{Y} denote the averages of the respective sequences. The PCC quantifies the linear correlation between two variables, serving as a numerical gauge of how closely the reconstructed wavefield matches the ground truth [39]. **Table 2** displays the computed PCC values at each time instance, providing a quantitative

evaluation of the accuracy of the reconstruction.

A high PCC value indicates a strong linear correlation between the reconstructed wavefield and the ground truth, reflecting a close match between the two datasets. By integrating the qualitative analysis of reconstructed wavefields from **Figs. 6, 7, and 8** with the quantitative assessment provided by the PCC values in **Table 2**, we managed to evaluate the performance of the PINNs method in reconstructing LU wavefields. The results of this evaluation clearly suggests the PINN managed to reconstruct the wavefield data accurately.

As shown in **Table 2**, the PCC values at all three time points reached 0.95, indicating that the accuracy of the reconstructed wavefield is 95 %. This demonstrates that using PINN for wavefield reconstruction is feasible.

5.2. Reconstruction of wavefield data with a scanning interval of $4/3\lambda$

Here we introduce the reconstruction results of wavefield data with the scanning interval of $4/3\lambda$. **Fig. 11** provides valuable insights into the convergence behavior of the PINNs model during training. In **Fig. 11**, although the PDE loss terms exhibits some significant fluctuations in the early stages, it is evident that the overall trend is downward and stabilizes later. Other loss terms show similar behavior, indicating that our results are improving throughout the training process.

Similar to **Section 5.1**, **Fig. 12** offers a detailed comparison between the true LU wavefield and the reconstructed wavefield using the PINNs method at the specific time instance, $t=14.08 \mu\text{s}$. In **Fig. 12a**, the LU wavefield with the scanning interval of $1/15 \lambda$, obtained through LU testing methods, serves as the ground truth, providing a reference for the reconstruction's accuracy. **Fig. 12b** depicts the LU wavefield with a scanning interval of $4/3 \lambda$, representing the input data used by the PINNs model. Compared to **Fig. 7b**, **Fig. 12b** is even more blurred, indicating that reconstructing the wavefield with a scanning interval of $4/3 \lambda$ is

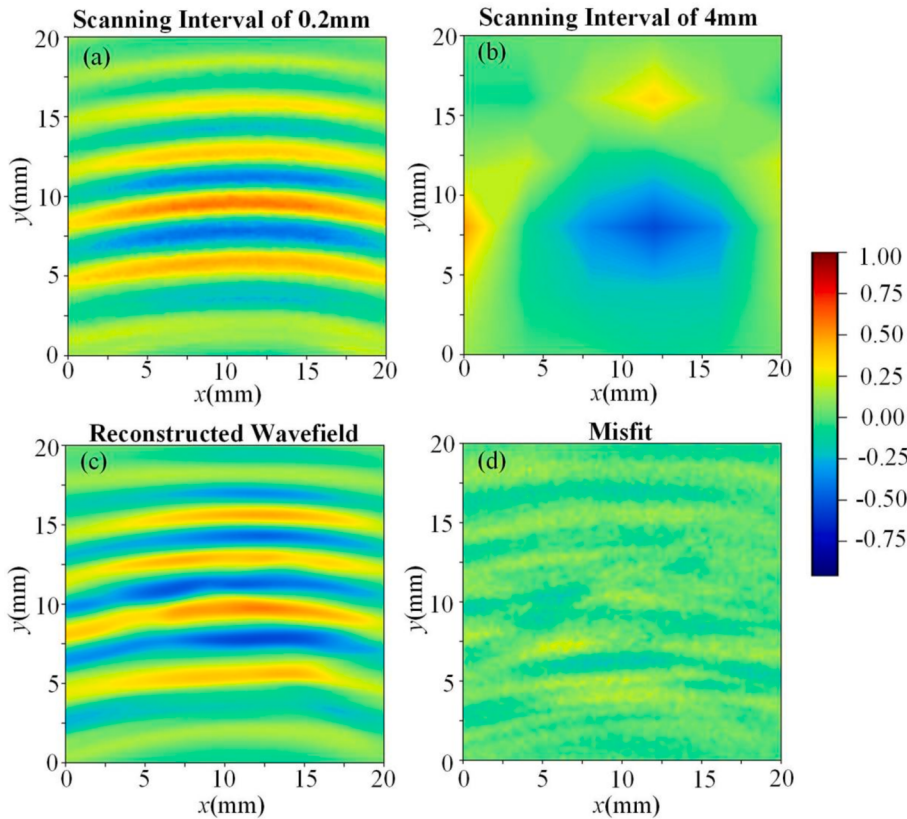


Fig. 14. Wavefield results at time instance $t = 15.36 \mu\text{s}$. (a) The wavefield with the scanning interval of $1/15 \lambda$, (b) the sparse wavefield with the scanning interval of $4/3 \lambda$ as the input data, (c) the reconstructed wavefield by PINNs, and (d) the absolute pointwise error between (a) the true wavefield and (c) reconstructed wavefield.

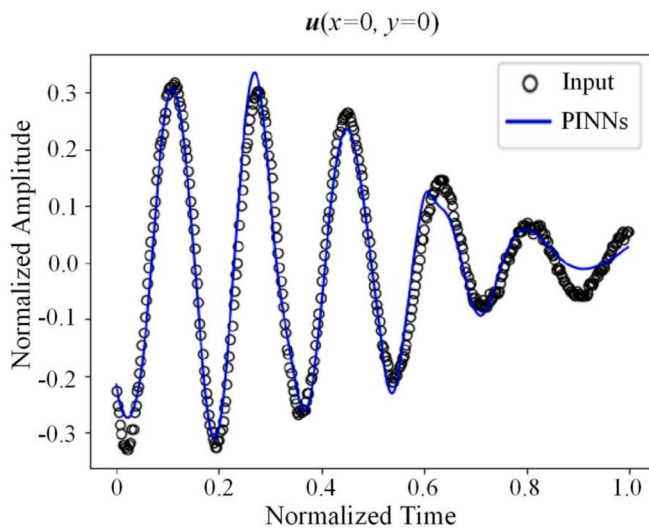


Fig. 15. The fitting results of the A-scan data at the first point among the 36 points selected of the wavefield. 'O' represents real data, the blue curve is the prediction of PINNs.

Table 3
Pearson correlation coefficients at different instance.

Time (μs)	14.08	14.72	15.36
PCC	0.957	0.954	0.957

more challenging. Fig. 12c displays the wavefield reconstructed by the PINNs. Compared to Fig. 7c, the waveforms in Fig. 12c appear less smooth. Fig. 12d shows the absolute pointwise error. Notably, the errors shown in Fig. 12d appear smaller compared to Fig. 7d. Fig. 12d does not display obvious error streaks, demonstrating the neural network's good stability and robustness.

Figs. 13 and 14 present the reconstructed wavefields at two additional time instances, $t=14.72 \mu\text{s}$ and $t = 15.36 \mu\text{s}$, respectively. Observing Fig. 13c and 14c, the reconstructed wavefields at these times still do not appear as smooth as those shown in Section 5.1. However, the errors displayed in Fig. 13c and 14c are smaller than those calculated in Section 5.1.

Fig. 15 offers insight into the fitting performance of the PINNs model with respect to the A-scan data collected at the first point among the sparse 6×6 points of the wavefield. As shown in Fig. 15, the results produced by the PINNs model exhibit good consistency with the input signals, demonstrating the neural network's strong capability even when handling limited data.

Similar to Section 5.1, we also provide the PCC results of the three moments, as shown in Table 3.

As we can see from Figs. 12, 13, and 14, PINNs also showed good reconstruction ability for wavefield with scanning interval of $4/3 \lambda$. However, the reconstructed waveform does not appear as smooth as the wavefield reconstruction results with scanning interval of $2/3 \lambda$. The reason could be that we selected fewer sampling points, and the wavefield data at these points do not fully comply with the partial differential equation [40]. Excitingly, as shown in Table 3, the PCC results at all three time points reached 0.95. For wavefield reconstruction with a scanning interval of $4/3 \lambda$, the PCC still achieved excellent results. Compared to the wavefield reconstruction results with a scanning interval of $2/3 \lambda$, the PCC results are even more outstanding at $t = 14.08 \mu\text{s}$ and $t = 15.36 \mu\text{s}$. This demonstrates that the constructed phys-

informed neural network can achieve good results in wavefield reconstruction even with less data. In addition, due to the small amount of input data, various loss functions in Fig. 11 declined faster, and the fitting results of A-scan data in Fig. 15 were also satisfactory. Overall, there was no deterioration in results due to a reduction in input data.

At this point, we have achieved the reconstruction of wavefields with scanning intervals of $2/3 \lambda$ and $4/3 \lambda$, with the reconstructed wavefield having an interval of $1/15 \lambda$. Analysis of the wavefield reconstruction results demonstrates that physics-informed neural networks can effectively identify the underlying physical laws within the wavefield data. This study demonstrates that, under certain conditions, a complete wavefield can be reconstructed even with a scanning interval of $4/3 \lambda$. This breaks the limitations of the traditional Nyquist sampling theorem. At the same time, due to the reduced number of sampling points, it effectively extends the lifespan of laser ultrasonic devices.

6. Conclusions

We managed to adopt the PINNs method to reconstruct the LU wavefield. To do so, we used two neural networks to predict the wavefield data and constrained both networks in the training using the available wavefield data and acoustic wave equation. Our study highlights the following key point:

We successfully used PINNs to reconstruct LU wavefields, even with LU experimental data. This method proved highly accurate, with correlation coefficients exceeding 0.95 between reconstructed and actual LU wavefields with scanning interval of $2/3 \lambda$ and correlation coefficients exceeding 0.95 between reconstructed and actual LU wavefields with scanning interval of $4/3 \lambda$.

Our results demonstrate the potential of PINNs in structural health monitoring, particularly in full wavefield reconstruction. Using the proposed framework, we can predict the entire wavefield of a structure based on data from sparse spatial locations. This approach can be further explored to better detect and locate damages with less data. Although this preliminary work mainly focuses on simple plates without any defects, our future work will extend this framework to predict wavefields in more complex environments with fewer samples.

CRediT authorship contribution statement

Bin Xu: Writing – original draft, Validation, Software, Methodology. **Yun Zou:** Writing – review & editing, Funding acquisition. **Gao Feng Sha:** Writing – review & editing. **Liang Yang:** Writing – review & editing. **Guixi Cai:** Writing – review & editing. **Yang Li:** Writing – review & editing, Software, Methodology, Funding acquisition, Conceptualization.

Funding

This research was funded by the National Natural Science Foundation of China under Grant 51705470, and the Henan Provincial Key Scientific Research Project of Higher Education Institutions (222102220025).

Declaration of competing interest

The authors declare that they have no known competing financial interests or personal relationships that could have appeared to influence the work reported in this paper.

Data availability

Data will be made available on request.

References

- [1] M.H. Lu, L. Ding, X.J. Yan, Application and prospect of laser ultrasonic nondestructive testing technology in advanced manufacturing[J], *J Vib Meas Diagn* 41 (4) (2021) 631–643.
- [2] M.F. Koldunov, A.A. Manenkov, I.L. Pokotilo, Thermoelastic and ablation mechanisms of laser damage to the surfaces of transparent solids[J], *Quantum Electron.* 28 (3) (1998) 269.
- [3] F. Qin, Y. Wu, H. Guo, et al., Laser ultrasonic nondestructive testing based on nonlinear ultrasonic coefficient[J], *Russ. J. Nondestr. Test.* 56 (2020) 209–221.
- [4] X. Tian, J. Zhao, B. Lu, et al., Laser Ultrasonic Quantitative Detection of Buried Depth for Internal Defects in Additive Manufacturing Parts [J], *China Mechanical Engineering* 33 (8) (2022) 952–959.
- [5] R. Arie, A. Brand, S. Engelberg, Compressive sensing and sub-Nyquist sampling[J], *IEEE Instrum. Meas. Mag.* 23 (2) (2020) 94–101.
- [6] O. Mesnil, M. Ruzzene, Sparse wavefield reconstruction and source detection using compressed sensing[J], *Ultrasonics* 67 (2016) 94–104.
- [7] S. Sabeti, J.B. Harley, Spatio-temporal undersampling: Recovering ultrasonic guided wavefields from incomplete data with compressive sensing [J], *Mech. Syst. Sig. Process.* 140 (2020).
- [8] P. Li, Y. Luo, Y. Zhou, et al., Application of compressed sensing in damage imaging by guided wavefield in metal plate[C]//2019 13th Symposium on Piezoelectricity, Acoustic Waves and Device Applications (SPAWDA), IEEE (2019) 1–5.
- [9] C. Liu, D. Wang, J. Sun, et al., Crossline-direction reconstruction of multi-component seismic data with shearlet sparsity constraint[J], *J. Geophys. Eng.* 15 (5) (2018) 1929–1942.
- [10] A. Gholami, A. Richardson, T. Zand, et al., Efficient wavefield reconstruction at half the Nyquist rate[J], *Geophysics* 84 (5) (2019) A43–A46.
- [11] M. Kalita, T. Alkhalifah, Common-image gathers using the excitation amplitude imaging condition[J], *Geophysics* 81 (4) (2016) S261–S269.
- [12] M. Kalita, T. Alkhalifah, Efficient full waveform inversion using the excitation representation of the source wavefield[J], *Geophys. J. Int.* 210 (3) (2017) 1581–1594.
- [13] K.S. Alguri, J.B. Harley, Transfer learning of ultrasonic guided waves using autoencoders: A preliminary study[C]//AIP conference proceedings, AIP Publishing 2102 (1) (2019).
- [14] M.M. Azad, P. Kumar, H.S. Kim, Delamination detection in CFRP laminates using deep transfer learning with limited experimental data[J], *J. Mater. Res. Technol.* 29 (2024) 3024–3035.
- [15] D. Ji, J. Lin, F. Gao, The high-sparsity Lamb wavefield reconstruction framework based on masked autoencoder[J], *IEEE Trans. Instrum. Meas.* (2023).
- [16] L. Herrmann, S. Kollmannsberger, Deep learning in computational mechanics: a review[J], *Comput. Mech.* (2024) 1–51.
- [17] M. Raissi, P. Perdikaris, G.E. Karniadakis, Physics-informed neural networks: A deep learning framework for solving forward and inverse problems involving nonlinear partial differential equations[J], *J. Comput. Phys.* 378 (2019) 686–707.
- [18] C. Song, T.A. Alkhalifah, Wavefield reconstruction inversion via physics-informed neural networks[J], *IEEE Trans. Geosci. Remote Sens.* 60 (2021) 1–12.
- [19] T. Alkhalifah, C. Song, U bin Waheed, et al., Wavefield solutions from machine learned functions constrained by the Helmholtz equation, *Artificial Intelligence Geosciences* 2 (2021) 11–19.
- [20] P. Ren, C. Rao, S. Chen, et al., SeismicNet: Physics-informed neural networks for seismic wave modeling in semi-infinite domain[J], *Comput. Phys. Commun.* 295 (2024) 109010.
- [21] M. Rasht-Behesht, C. Huber, K. Shukla, et al., Physics-informed neural networks (PINNs) for wave propagation and full waveform inversions[J], *Journal of Geophysical Research: Solid Earth* 127 (5) (2022) e2021JB023120.
- [22] Y. Ding, S. Chen, X. Li, et al., Self-adaptive physics-driven deep learning for seismic wave modeling in complex topography[J], *Eng. Appl. Artif. Intel.* 123 (2023) 106425.
- [23] S. Cheng, T. Alkhalifah, Robust data driven discovery of a seismic wave equation [J], *Geophys. J. Int.* 236 (1) (2024) 537–546.
- [24] X. Huang, T.A. Alkhalifah, Microseismic source imaging using physics-informed neural networks with hard constraints[J], *IEEE Trans. Geosci. Remote Sens.* 62 (2024) 1–11.
- [25] F. Brandolini, M. Ravasi, T. Alkhalifah, PINNslope: seismic data interpolation and local slope estimation with physics informed neural networks[J], *Geophysics* 89 (4) (2024) V331–V345.
- [26] I.A. Viktorov, *Rayleigh and Lamb Waves: Physical Theory and Applications*, Plenum Press, 1967.
- [27] K. Shukla, A.D. Jagtap, J.L. Blackshire, et al., A Physics-Informed Neural Network for Quantifying the Microstructural Properties of Polycrystalline Nickel Using Ultrasound Data: A promising approach for solving inverse problems [J], *IEEE Signal Process Mag.* 39 (1) (2022) 68–77.
- [28] S. Cho, W. Choi, J. Ji, et al., Analysis on Strategies for Modeling the Wave Equation with Physics-Informed Neural Networks[J], *Geophysics and Geophysical Exploration* 26 (3) (2023) 114–125.
- [29] Y. Ding, S. Chen, X. Li, et al., Physics-constrained neural networks for half-space seismic wave modeling [J], *Comput. Geosci.* 181 (2023).
- [30] A.G. Baydin, B.A. Pearlmutter, A.A. Radul, et al., Automatic differentiation in machine learning: a survey[J], *J. Mach. Learn. Res.* 18 (153) (2018) 1–43.
- [31] Abadi M, Barham P, Chen J, et al. {TensorFlow}: a system for {Large-Scale} machine learning[C]//12th USENIX symposium on operating systems design and implementation (OSDI 16). 2016: 265–283.

- [32] A.D. Jagtap, K. Kawaguchi, K.G. Em, Locally adaptive activation functions with slope recovery for deep and physics-informed neural networks[J], Proceedings of the Royal Society A 476 (2239) (2020) 20200334.
- [33] Datta L, A survey on activation functions and their relation with xavier and he normal initialization[J]. arXiv preprint arXiv:2004.06632, 2020.
- [34] Y. Tian, Y. Zhang, H. Zhang, Recent advances in stochastic gradient descent in deep learning[J], Mathematics 11 (3) (2023) 682.
- [35] R.H. Byrd, S.L. Hansen, J. Nocedal, et al., A stochastic quasi-Newton method for large-scale optimization[J], SIAM J. Optim. 26 (2) (2016) 1008–1031.
- [36] H. Nosrati, N.M. Emami, Manipulating the loss calculation to enhance the training process of physics-informed neural networks to solve the 1D wave equation[J], Eng. Comput. 40 (3) (2024) 1741–1769.
- [37] I.M. Sobol', On the distribution of points in a cube and the approximate evaluation of integrals[J], Zhurnal Vychislitel'noi Matematiki i Matematicheskoi Fiziki 7 (4) (1967) 784–802.
- [38] J. Kalina, P. Vidnerová, Properties of the weighted and robust implicitly weighted correlation coefficients[C]//International Conference on Artificial Neural Networks, Springer Nature Switzerland, Cham, 2023, pp. 200–212.
- [39] P. Schober, C. Boer, L.A. Schwarte, Correlation coefficients: appropriate use and interpretation[J], Anesth. Analg. 126 (5) (2018) 1763–1768.
- [40] L. Yang, X. Meng, G.E. Karniadakis, B-PINNs: Bayesian physics-informed neural networks for forward and inverse PDE problems with noisy data[J], J. Comput. Phys. 425 (2021) 109913.